

DNA Nanostructures Coordinate Gene Silencing in Mature Plants

Huan Zhang^{1,§}, Gozde S. Demirer^{1,§}, Honglu Zhang^{2,§}, Tianzheng Ye¹, Natalie S. Goh¹, Abhishek J. Aditham¹, Francis J. Cunningham¹, Chunhai Fan^{3,4}, and Markita P. Landry^{1,5,6,7*}

¹ Department of Chemical and Biomolecular Engineering, University of California, Berkeley, CA 94720, USA.

² Department of Molecular and Cell Biology, University of California, Berkeley, CA 94720, USA.

³ Division of Physical Biology & Bioimaging Center, Shanghai Synchrotron Radiation Facility, CAS Key Laboratory of Interfacial Physics and Technology, Shanghai Institute of Applied Physics, Chinese Academy of Sciences, Shanghai 201800, China.

⁴ School of Chemistry and Chemical Engineering, Shanghai Jiao Tong University (SJTU), Shanghai, 200240, China.

⁵ Innovative Genomics Institute (IGI), Berkeley, CA 94720, USA.

⁶ California Institute for Quantitative Biosciences, QB3, University of California, Berkeley, CA 94720, USA.

⁷ Chan-Zuckerberg Biohub, San Francisco, CA 94158, USA.

[§] Authors contributed equally to this work.

*e-mail: landry@berkeley.edu

Nanostructure design and synthesis considerations

Three DNA nanostructures with programmed sizes and shapes were synthesized: tetrahedron, hairpin-tile (HT) monomer, and nanostring, as illustrated in Figure 1. Both the HT monomer and tetrahedron were assembled with four single stranded DNA oligonucleotides with complementary sequences to form the desired nanostructure size and shape (See Supplementary Table S1 for DNA sequences). Briefly, the tetrahedron DNA sequences were designed to create a final tetrahedron shape (triangular pyramid) with 2.4 nm, 8.8 nm, or 12.6 nm edges when assembled through annealing of four pre-designed single stranded DNA oligonucleotides. The HT monomer was designed to contain a sticky end and a stem-loop hairpin structure, enabling co-polymerization with another monomer to assemble into the length-controlled 1D nanostring by introduction of an initiator (Fig. S1 and S2).

In detail, the initiator can open the hairpin loop structure of the monomer A through a toehold-mediated strand displacement reaction to produce a complex carrying a reactive terminus (I-A). The reactive terminus can invade the hairpin domain of monomer B and activate it with an exposed sequence identical to I (I-A-B), which will further activate monomer A. Subsequently, copolymeric chain growth happens exclusively with sequential addition of monomers A and B to these active termini until monomers are consumed. We can tune the molar ratio of initiator I to monomers A and B to control the final average length of the nanostring. For the nanostring we employed in this study, the molar ratio of monomer to initiator was 10. As such, only 10% of monomers are activated by the initiator, followed by the chain growth reaction, until all monomers are consumed to form the nanostring with an average length of 10 monomer subunits. As such, we can tune the final length of the nanostring by changing the molar ratios of monomers with initiator I by keeping the concentration of monomers constant. As with any chain-growth polymerization reaction, it is common to obtain a distribution of lengths for the final product. In Fig. S3, we show the length distribution of HT monomer and nanostring, which follows a Gaussian distribution with mean lengths of 16 nm and 312 nm, respectively.

Cost calculation and considerations for DNA nanostructures

DNA nanostructures are relatively inexpensive when compared to other methods of siRNA delivery (for example gene gun). We calculated the cost of one infiltration (100 nM, 100 μ l) for silencing with different nanostructures used in this study to estimate the cost and scalability of our DNA nanostructure platform (Supplementary Table S3). We find that the total cost of one silencing experiment with tetrahedron, HT monomer, or nanostring is less than one US dollar (\$0.53, \$0.58 and \$0.65, respectively), which is comparatively affordable and is amenable for scale-up if needed. However, we show that the cost is significantly higher for the 8-helix bundle origami for one silencing experiment (\$50) due to the high cost of DNA materials to form the 8-helix bundle structure.

Calculation of relative nanostructure bending stiffness

The bending stiffness (k_b) of a beam-shaped structure is described by:

$$k_b = \frac{3EI}{L^3}$$

where E is Young's modulus (elastic modulus), L is the length of the DNA nanostructure, and I is the area moment of inertia.

To estimate the moment of inertia, we treat a 1D nanostructure as a bundle of N rigidly linked cylindrical rods of radius r , where I can be calculated in terms of $I(1, 2)$. The moment of inertia of each dsDNA helix with respect to its own center of mass is i , and is displaced from the nanostructure's center of mass by a distance R . By the parallel axis theorem, the moment of inertia of the dsDNA helix with respect to the nanostructure's center of mass is $i+MR^2$, where M is the mass of the helix. Assuming uniform density,

$$i = \frac{1}{2}Mr^2$$

and thus

$$I = N(i + MR^2) = N\left(i + 2i\frac{R^2}{r^2}\right)$$

with Relative stiffness (see Table S2)

$$\frac{k_b(\text{nanostructure})}{k_b(\text{dsDNA})} = \frac{I}{i} \times \left(\frac{L(\text{dsDNA})}{L(\text{nanostructure})}\right)^3 = N\left(1 + 2\frac{R^2}{r^2}\right) \times \left(\frac{L(\text{dsDNA})}{L(\text{nanostructure})}\right)^3$$

Structural conformation and mechanical stiffness simulation

The structural shape and mechanical compliance of siRNA, HT monomer, and nanostring were modeled using the finite element model with CanDo (cando-dna-origami.org) to predict the structural shape and mechanical flexibility of the DNA nanostructures. The nanostructures were modeled as homogeneous elastic rods with isotropic bending stiffness. The structural and mechanical parameters of the two-node beam finite elements composing each rod are:

- B-form DNA helix is modeled as a worm-like chain.
- Axial length per base pair: 0.34 nm;
- Helical diameter: 2.25 nm;
- Base pairs per turn: 10.5;
- Bending stiffness: 230 pN·nm²;

- Stretching modulus: 1100 pN;
- Torsional stiffness: 460 pN·nm².

The backbone bending and torsional stiffness are reduced by 100-fold when there are nicks in the DNA double helix, and thus single-stranded DNA present as sticky ends or loops are modeled as entropic springs using a modified freely jointed chain model. Interhelical crossovers are treated as rigid components with zero length.

The structural conformation and mechanical stiffness of DNA nanostructures at the ground-state solution are performed by a normal mode analysis with CanDo. Thermal fluctuations are quantified by computing root-mean-square fluctuations (RMSF) of base pairs at a temperature of 298 K. Here, RMSF measures the magnitude of motion of base pairs and resulting flexibility of DNA nanostructures.

Calculation of nanostructure compactness

The compactness of a 3D structure relates the enclosing surface area (A) with the volume (V) and can be defined by the area^{1.5}/volume ratio, which is dimensionless and can be minimized by a sphere.

The compactness of 3D structure

$$C_{structure} = A^{1.5}/V$$

For a sphere:

$$A_{sphere} = 4\pi r^2$$

$$V_{sphere} = \frac{4}{3}\pi r^3$$

The compactness of sphere

$$\begin{aligned} C_{sphere} &= A_{sphere}^{1.5}/V_{sphere} \\ &= 3\sqrt{4\pi} \end{aligned}$$

Which is the minimum compactness of a solid since the sphere encloses maximum volume for a constant surface area.

The compactness is defined as

$$C = C_{sphere}/C_{structure}$$

C_{sphere} is the calculated value of a sphere, and $C_{structure}$ is the calculated value of the sphere DNA nanostructures.

DNA nanostructure toxicity analysis

Most prior work comes to a consensus that DNA based nanostructures do not exhibit toxicity in mammalian systems (3, 4). Since DNA nanostructures have not been used in plant systems to-date, we assessed whether DNA nanostructures are biocompatible in plants. Specifically, we monitored the expression of the respiratory burst oxidase homolog B (NbrbohB) gene, which is a known stress gene upregulated under broad types of biotic and abiotic stress in *Nicotiana Benthamiana* (*Nb*) plants (5). Following infiltration of *Nb* leaves with either PBS buffer or nanostructures, NbrbohB mRNA was measured and normalized with respect to the Elongation Factor 1 (EF1) housekeeping gene. As summarized in Figure S22, leaves infiltrated with either of the DNA nanostructures does not result in NbrbohB gene upregulation compared to adjacent areas within the same leaf treated only with PBS buffer. Furthermore, the structural integrity of the plant cells is unperturbed by introduction of the various DNA nanostructures (Figure 2, 3, 4, and SI Appendix, Figure S5, S6, S8, S11). Our analyses suggest that DNA nanostructures do not induce a stress response in plants and are a biocompatible mode of siRNA delivery to plant cells.

Supplementary Table S1 | Sequences of oligonucleotides used in this study.

Name	Sequence (5'-3')
H1	GGACTTGTAGCGATACGACTCCGACGAGACTAGTAACTCTTG
H2	GGATGCGGAATGACAGCTACAAGTCCCAAGAGTTACGCTCTCCATTC
H3	TGTCACAGTAAGTCTTGTCATTCC
H4	GGGCTTGAATGGAGAGCCATCACTCATGTGAACCCATGAGTGATGTAGTCTCGTCGGAGTCGT ATCAGACTTACT
H5	ACGAGACTACATGGTCAGATTCGTAGGTCCGATACGACTCCG
H6	GCATCCGATCCGTCCTGTCTCGGACCTACGAATCTGACCACCGAGAATC
H7	AAGCCCGATTCTCGGTCACTCATGGGTTCA
H8	CATGAGTGATGTAGTCTCGTCGGAGTCGTATCAGACTTACTGTGACAAGTAAGTCTGACAGGA CGGATC
I	CATGAGTGATGTAGTCTCGTCGGAGTCGTATCAGACTTACTGTGACA
Bio-H1	Biotin-GGACTTGTAGCGATACGACTCCGACGAGACTAGTAACTCTTG
Cy3-H1	Cy3-GGACTTGTAGCGATACGACTCCGACGAGACTAGTAACTCTTG
H1-15- RNA	TAC ACG CAT CCT TAG GGACTTGTAGCGATACGACTCCGACGAGACTAGTAACTCTTG

H2-15-RNA	TAC ACG CAT CCT GGA TGC GGA ATG ACA TGC TAC AAG TCC CAA GAG TTA CGC TCT CCA TTC
H5-15 - CNT	ACGAGACTACATGGTCAGATTTCGTAGGTCCGATACGACTCCG TAC ACG CAT CCT TAG
A-7	GAGCGTT A GCCACAC A CACAGTC
B-7	TTAGGCG A GTGTGGC A GAGGTGT
C-7	CGCCTAA A CAAGTGG A GACTGTG
D-7	AACGCTC A CCACTTG A ACACCTC
A-7-Cy3	GAGCGTT A GCCACAC A CACAGTC-Cy3
A-15-RNA	G CAT CCT TAG AAA AAA GAGCGTT A GCCACAC A CACAGTC
sense-15	CTA AGG ATG CGT GTA GGU GAU GCA ACA UAC GGAA TT
antisense	UUC CGU AUG UUG CAU CACC
(GT)₁₅₋₁₅	GTGTGTGTGTGTGTGTGTGTGTGTGTGTGTGT CTA AGG ATG CGT GTA
(GT)₁₅₋₁₅-Cy3	GTGTGTGTGTGTGTGTGTGTGTGTGTGTGTGT CTA AGG ATG CGT GTA-Cy3
fGFP	AGTGGAGAGGGTGAAGGTGATG
rGFP	GCATTGAACACCATAAGAGAAAGTAGTG
fEF1	GCATTGAACACCATAAGAGAAAGTAGTG
rEF1	ACGCTTGAGATCCTTAACCGCAACATTCTT
fNbrbohB	TTTCTCTGAGGTTTGCCAGCCACCACCTAA
rNbrbohB	GCCTTCATGTTGTTGACAATGTCTTTAACA
A-26	GCC TGG AGA TAC ATG CAC ATT ACG GCT TTC CCT ATT AGA AGG TCT CAG GTG CGC GTT TCG GTA AGT AGA CGG GAC CAG TTC GCC
B-26	CGC GCA CCT GAG ACC TTC TAA TAG GGT TTG CGA CAG TCG TTC AAC TAG AAT GCC CTT TGG GCT GTT CCG GGT GTG GCT CGT CGG
C-26	GGC CGA GGA CTC CTG CTC CGC TGC GGT TTG GCG AAC TGG TCC CGT CTA CTT ACC GTT TCC GAC GAG CCA CAC CCG GAA CAG CCC
D-26	GCC GTA ATG TGC ATG TAT CTC CAG GCT TTC CGC AGC GGA GCA GGA GTC CTC GGC CTT TGG GCA TTC TAG TTG AAC GAC TGT CGC
A-26-Cy3	GCC TGG AGA TAC ATG CAC ATT ACG GCT TTC CCT ATT AGA AGG TCT CAG GTG CGC GTT TCG GTA AGT AGA CGG GAC CAG TTC GCC-Cy3
A-37-1	CCC TGT ACT GGC TAG GAA TTC ACG TTT TAA TCT GGG CTT TGG GTT AAG AAA CTC CCC G

A-37-2	CGC TGG AGG CGC ATC ACC GTT TGC GTA TGT GTT CTG TGC GGC CTG CCG TCC CGT GTG GG
B-37-1	CGG TGA TGC GCC TCC AGC GCG GGG AGT TTC TTA ACC CTT TCC GAC TTA CAA GAG CCG G
B-37-2	GCG AGA CTC AGG TGG TGC CTT TGG CAT TCG ACC AGG AGA TAT CGC GTT CAG CTA TGC CC
C-37-1	CCC ATG AGA ATA ATA CCG CCG ATT TAC GTC AGT CCG GTT TCC CAC ACG GGA CGG CAG GC
C-37-2	CGC ACA GAA CAC ATA CGC TTT GGG CAT AGC TGA ACG CGA TAT CTC CTG GTC GAA TGC C
D-37-1	GCC CAG ATT AAA ACG TGA ATT CCT AGC CAG TAC AGG GTT TCC GGA CTG ACG TAA ATC GG
D-37-2	CGG TAT TAT TCT CAT GGG TTT GGC ACC ACC TGA GTC TCG CCC GGC TCT TGT AAG TCG G
A-37-1-Cy3	Cy3-CCC TGT ACT GGC TAG GAA TTC ACG TTT TAA TCT GGG CTT TGG GTT AAG AAA CTC CCC G

Supplementary Table S2 | Calculation of nanostructure parameters

Structures	Cross-section (nm ²)	Length (nm)	Relative stiffness ($k_{\text{structure}}/k_{\text{ds DNA}}$)	Compactness ($C_{\text{structure}}/C_{\text{sphere}}$)	Co-localization fraction	Aspect ratio w/ siRNA	
HT monomer	2 × 5	16	0.83	0.45	59.5 ± 1.5%	Center	1:1
						Side	5:1
Nanostring	2 × 5	320	1.0×10^{-4}	0.11	35.8 ± 0.9%	20:1	
8-helix bundles	6 × 7.2	300	1.7×10^{-3}	0.19	52.7 ± 1.1%	-	
SWCNT	1 × 1	~500	GPa to TPa (6, 7)	-	54.2 ± 4.5 %	35:1	
Tetrahedron-7	-	2.4	-	0.55	54.4 ± 2.7 %	5:1	
Tetrahedron-26	-	8.8	-	0.55	47.7 ± 0.6 %	-	
Tetrahedron-37	-	12.6	-	0.55	36.6 ± 1.6 %	-	

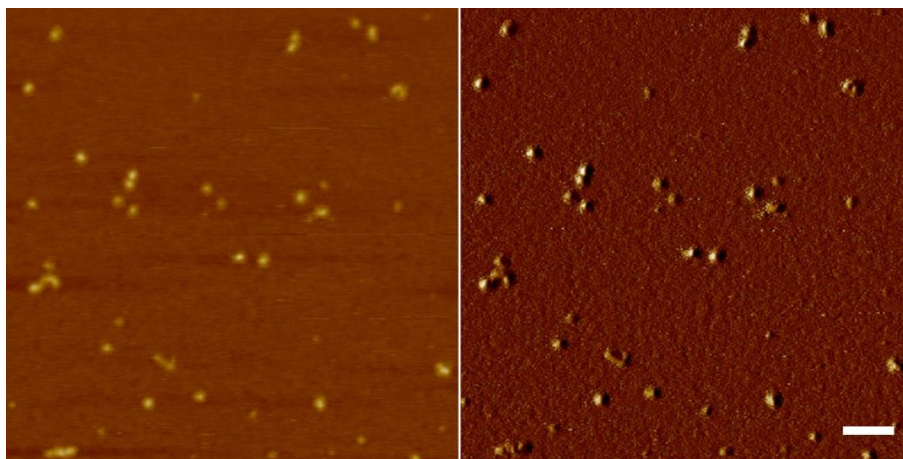


Figure S2. 2.4 nm tetrahedron nanostructure imaging. AFM images of tetrahedron nanostructures. Left: height image; Right: phase image. Scale bar: 100 nm.

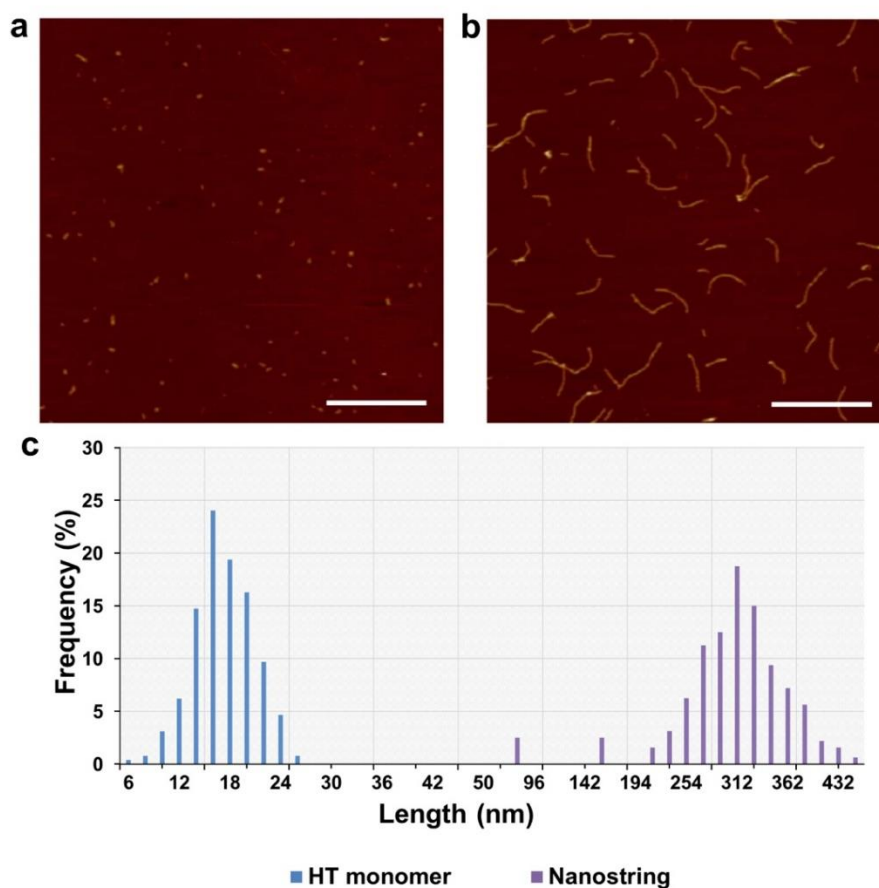


Figure S3. HT monomer and nanostring length distributions. AFM height images of (a) HT monomer and (b) nanostring nanostructures. Scale bar: 500 nm. c) Statistical analysis of the HT monomer and nanostring length distribution from AFM images.



Figure S4. DNA nanostructure infiltration procedure. A small puncture on the abaxial surface of the leaf lamina was introduced with a pipette tip, and $\sim 100 \mu\text{L}$ of the solution was infiltrated from the hole with a 1 mL needleless syringe by applying a gentle pressure, with caution not to damage the leaf.

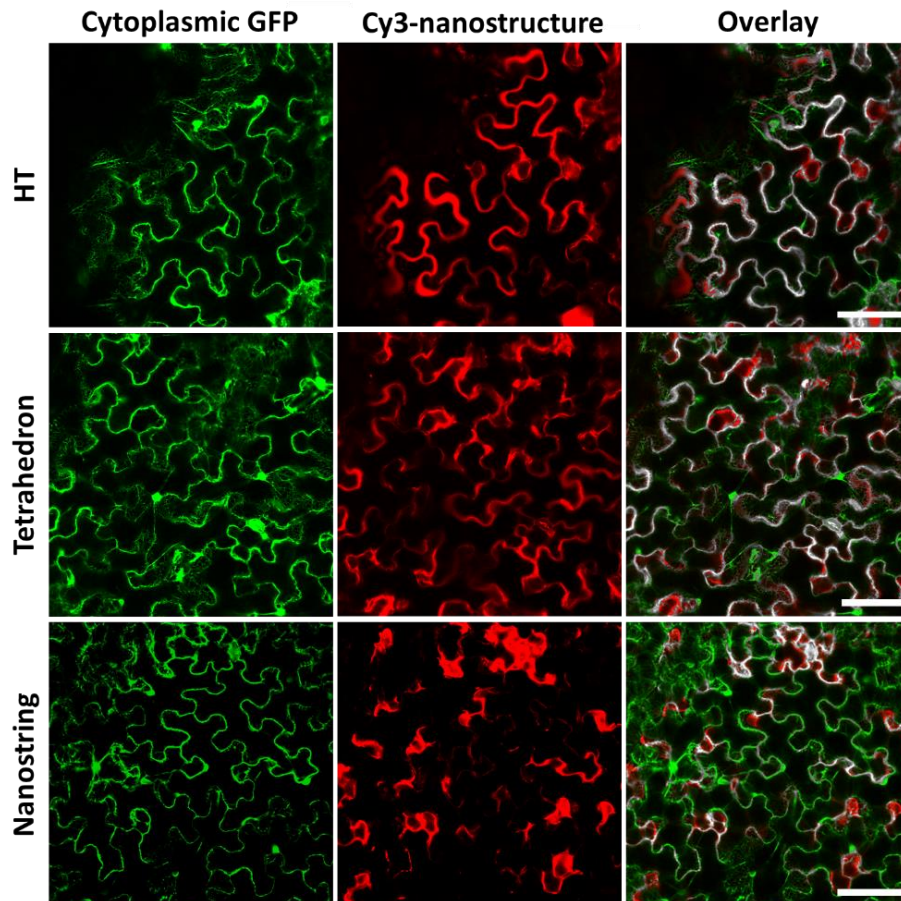


Figure S5. Internalization propensity of HT, tetrahedron, and nanostring nanostructures. Representative confocal images of Cy3 labeled HT monomer, tetrahedron, and nanostring co-localized with the GFP cytoplasm of mGFP5 *Nb*. Scale bars, 100 μm .

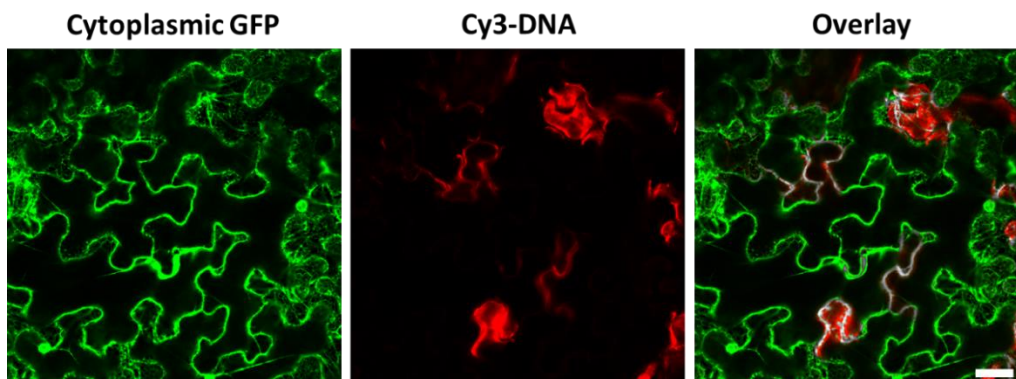


Figure S6. Free Cy3-labeled DNA oligonucleotides do not internalize into plant cells. Representative confocal images of Cy3 labeled single stranded DNA colocalized with the GFP cytoplasm of mGFP5 *Nb*. Scale bars, 50 μm .

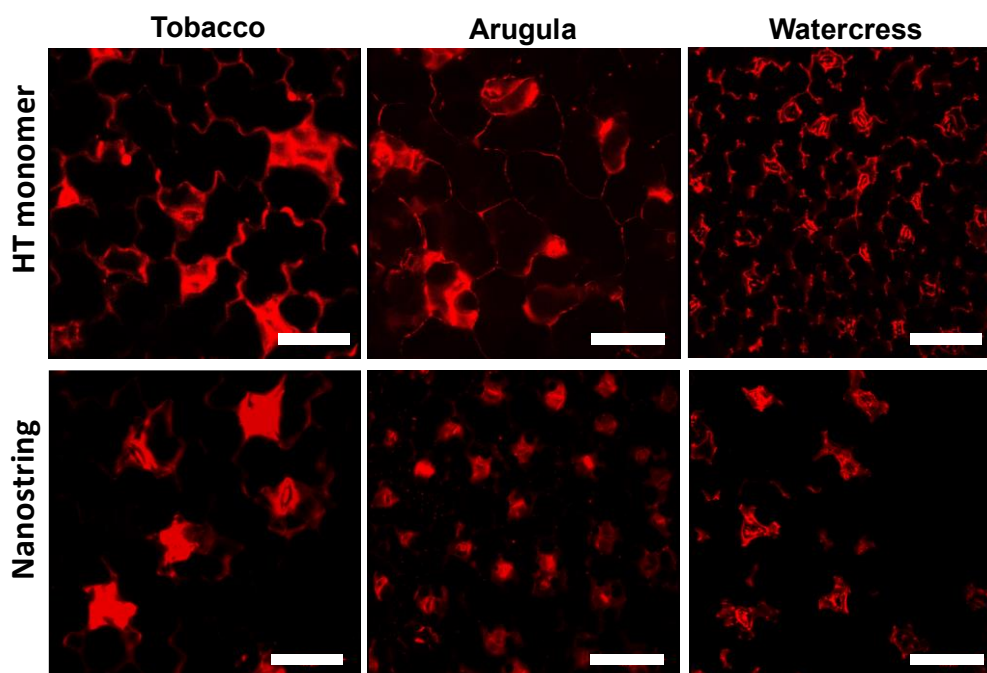


Figure S7. Internalization of Cy3 labeled HT monomer and Cy3 labeled nanostring into three different plant species. Cy3-labeled HT monomer can internalize into tobacco, arugula, and watercress leaf cells, whereas the nanostring appears to be retained in the leaf guard cells and shows limited cellular internalization across all species tested. Scale bars, 100 μm .

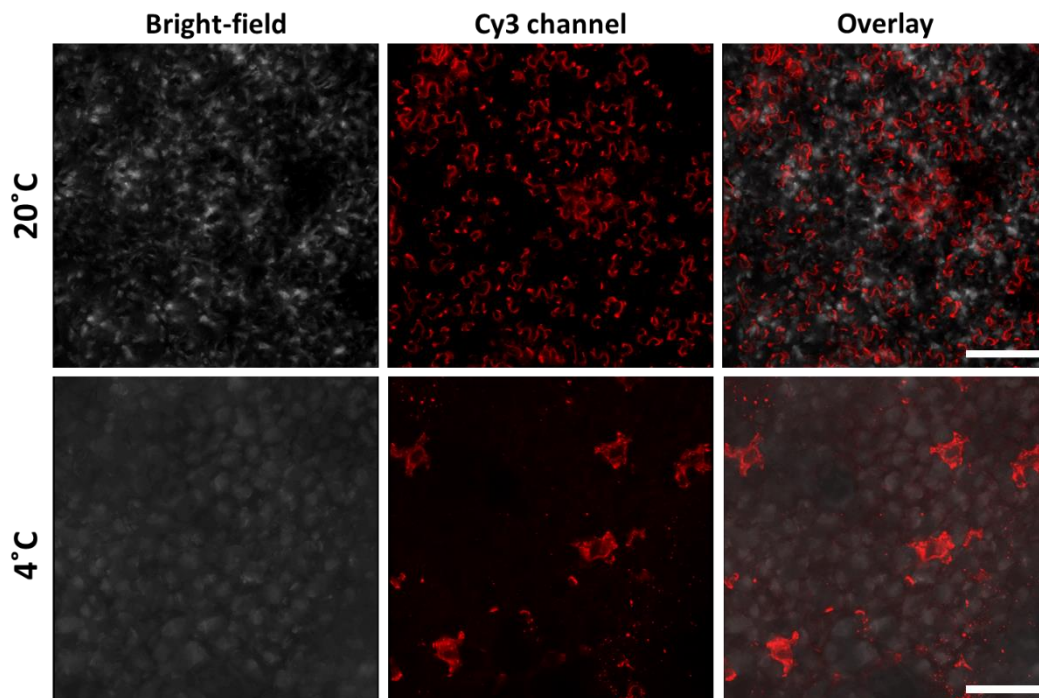


Figure S8. Nanostructure internalization into plant cells is temperature-dependent. Representative confocal images showing the temperature dependence of nanostructure internalization for the Cy3 labeled HT monomer. Scale bars, 50 μm .

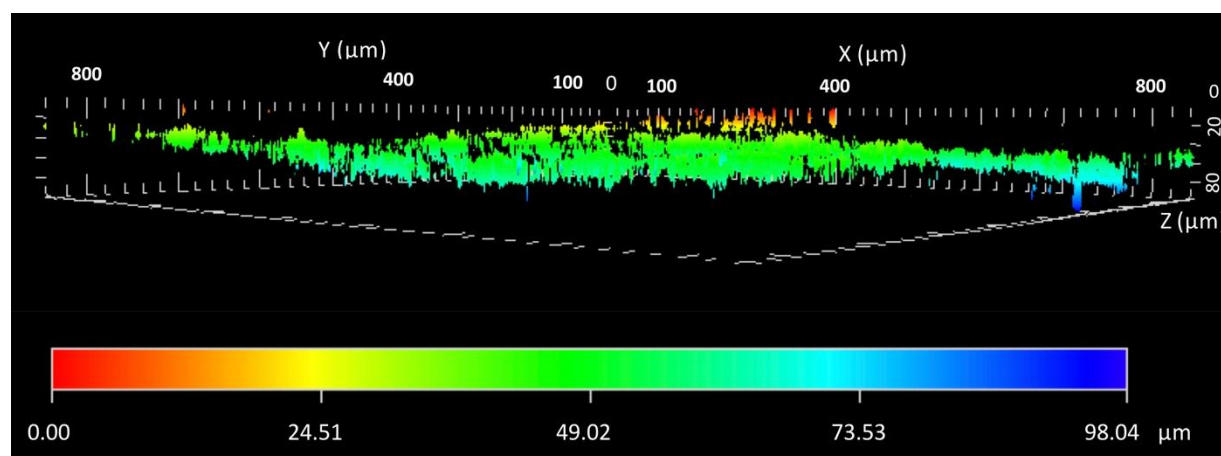


Figure S9. 3D z-stack analysis of the fluorescence profile of a Cy3 labeled HT monomer treated *Nb* leaf. Fluorescence originates from and diffuses $\sim 50 \mu\text{m}$ into the leaf tissue (z direction), and 2-3 cm in the x,y direction for a 100 μl infiltration.

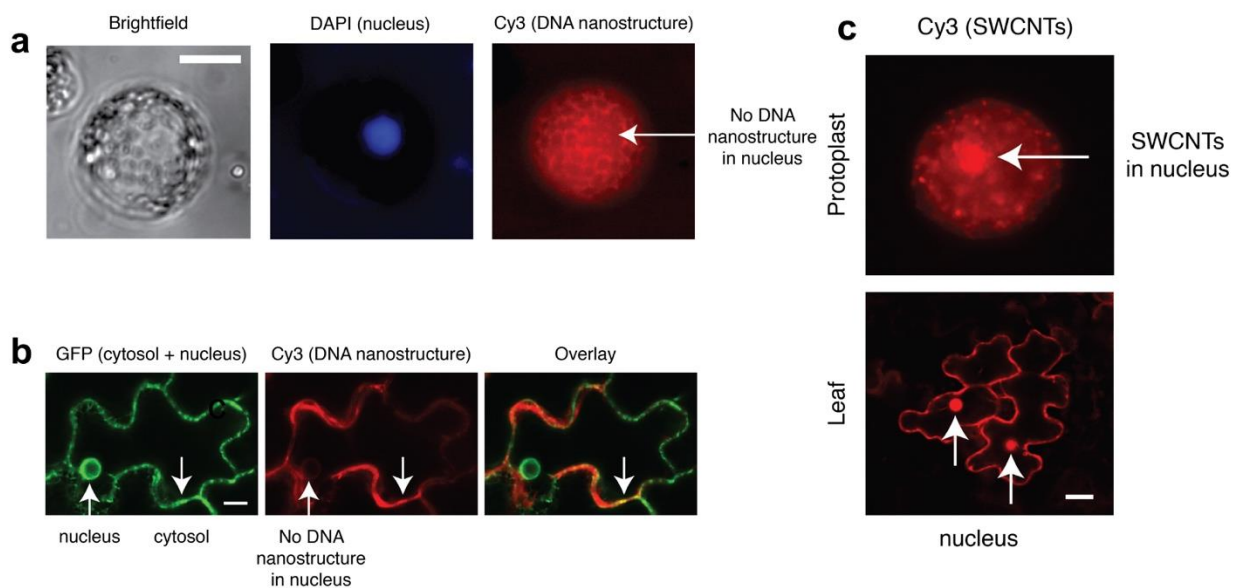


Figure S10. Subcellular localization of DNA nanostructures. a) Cy3-labeled DNA nanostructures localize in the cell cytosol of *Nb* protoplasts and are excluded from the nucleus. Scale bar: 20 μm . b) High resolution confocal co-localization shows that Cy3-labeled DNA nanostructures infiltrated into mGFP5 *Nb* leaves only enter the cytosol of plant cells, and no nanostructures are observed in the nucleus. Scale bar: 20 μm . c) Cy3-labeled SWCNTs (to compare with DNA nanostructures) in protoplasts and intact leaves show SWCNTs can enter both the cell cytosol and nucleus 6-hours post-co-incubation and post-infiltration, respectively. Scale bar: 25 μm

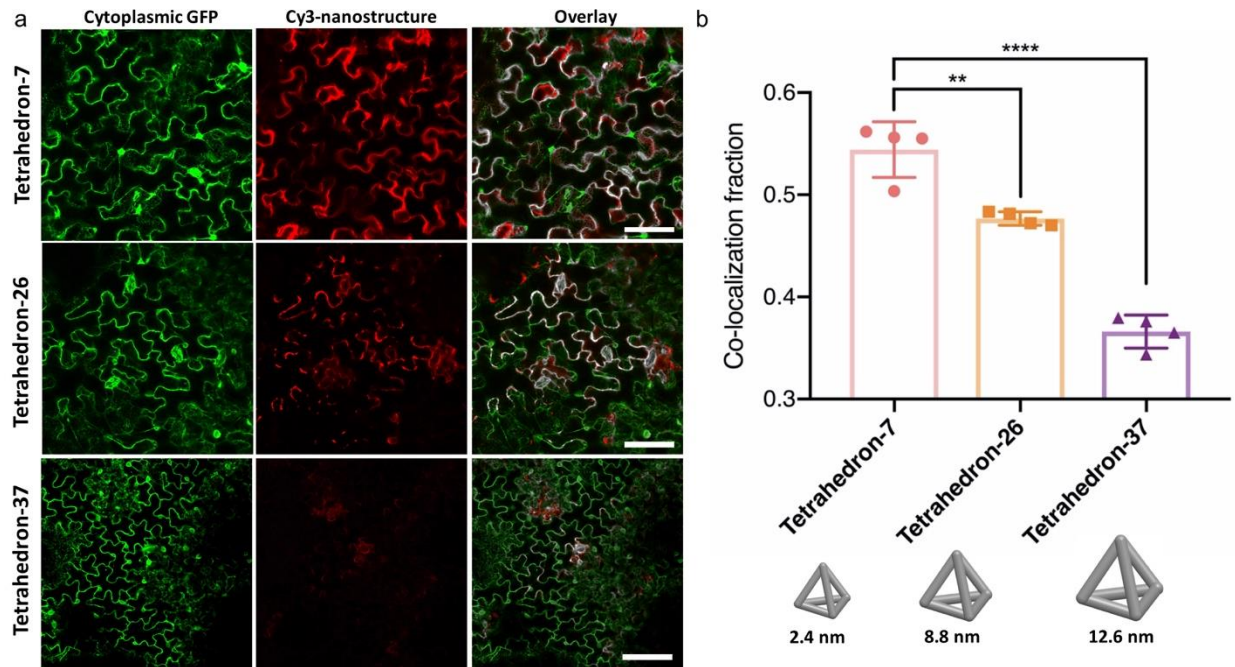


Figure S11. Cy3-labeled tetrahedron DNA nanostructure internalization into mGFP5 *Nb* leaf cells is size-dependent. a) Representative post-infiltration confocal images of 2.4 nm, 8.8 nm, or 12.6 nm Cy3-labeled tetrahedron nanostructures in mGFP5 *Nb* leaves. Tetrahedron nanostructure size is inversely proportional to cellular internalization. Scale bars, 100 μ m. b) Co-localization fraction of Cy3 fluorescence (nanostructure) with GFP fluorescence (plant cell cytosol) 12-hours post-infiltration into mGFP5 *Nb* leaves. $P^{**} = 0.0016$ and $P^{****} < 0.0001$ in one-way ANOVA. Error bars indicate s.e.m. ($n = 4$).

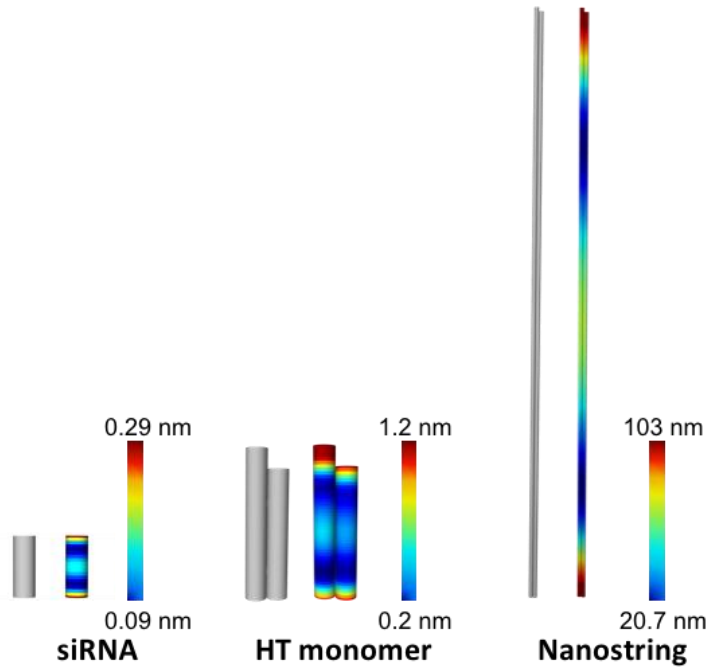


Figure S12. Simulation of DNA nanostructure bending stiffness. Equilibrium conformation and heat map color range of root-mean-square fluctuations (RMSF) for the siRNA, HT monomer, and nanostring nanostructures, simulated by CanDo (8, 9). Blue and red represent low and high relative flexibility, respectively. Bluest = 0% RMSF and reddest = 95% RMSF.

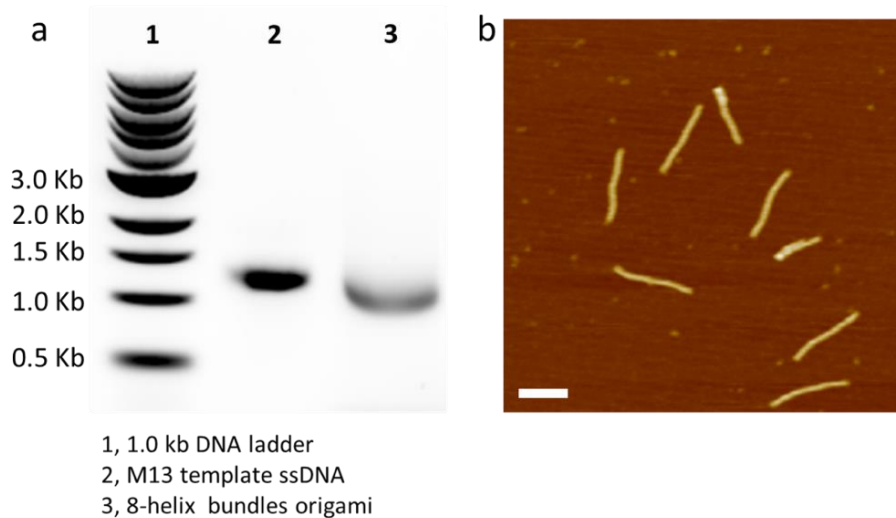


Figure S13. Validation of 8-helix DNA origami assembly. a) 1% agarose gel confirming the successful assembly of 8-helix bundle DNA origami. b) AFM image of 8-helix bundle DNA origami. Scale bar, 200 nm.

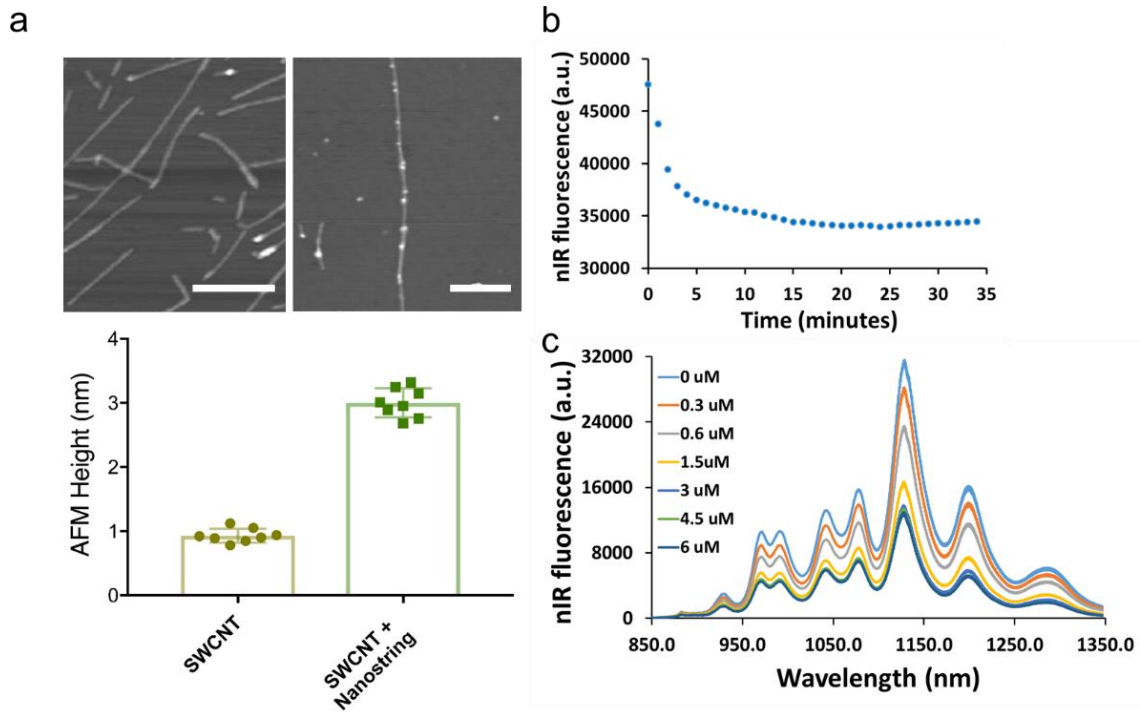


Figure S14. Confirmation of nanostring tethering to SWCNT. a) Representative AFM images of single-walled carbon nanotubes (SWCNT, upper left), SA-biotin nanostring conjugated SWCNT (upper right), and statistical height analysis of SWCNT (~1 nm) and SWCNT-nanostring conjugation (~3 nm). Scale bars, 100 nm. b) SWCNT nIR fluorescence change with time when nanostrings hybridize to SWCNTs. c) SWCNT nIR spectra after adding different nanostring concentrations, each spectrum was taken 10 minutes following nanostring addition.

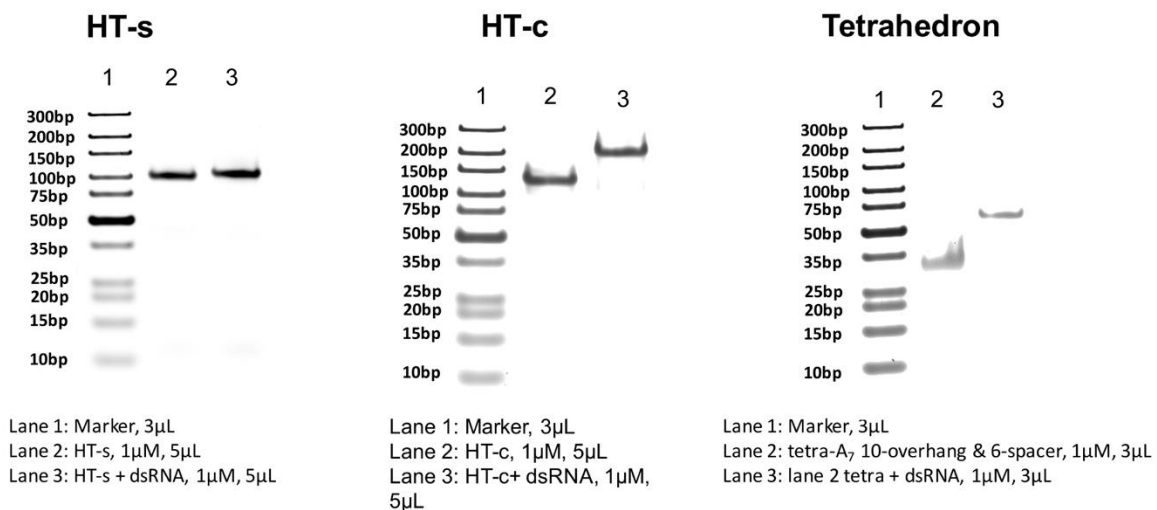


Figure S15. Validation of HT-s, HT-c, and tetrahedron attachment of siRNA. 10% Native-PAGE gels to verify attachment of siRNA to HT monomer and tetrahedron at different loci.

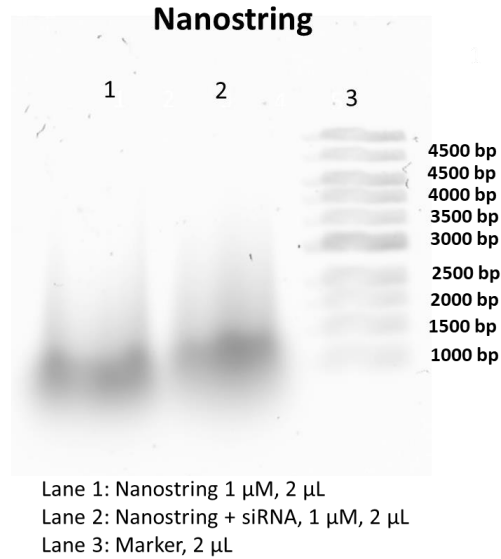


Figure S16. Validation of nanostring attachment of siRNA. 1% agarose gel confirming attachment of siRNA to nanostring.

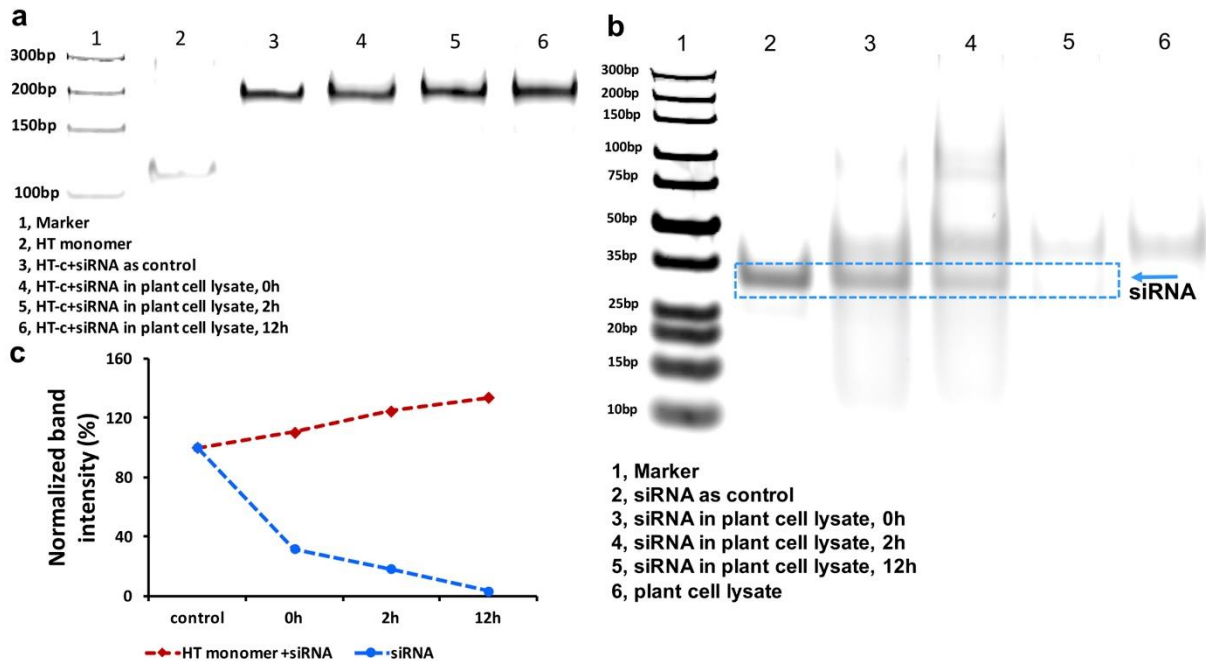


Figure S17. DNA nanostructures protect siRNA from nuclease degradation in plant cell lysate.

a) 10% Native-PAGE gel showing of siRNA attached to HT monomer and exposed to plant cell lysate, showing protection from degradation. b) siRNA alone is fully degraded 12 hours following exposure to plant cell lysate, but siRNA tethered to HT monomer is protected from degradation. c) Normalized band intensity analysis of the gels in part a) and b) where 100% band intensity is defined as the siRNA without the plant cell lysate. Upward deviations from 100% are due to nonspecific protein adsorption to nanostructures slightly increasing the band width and optical density.

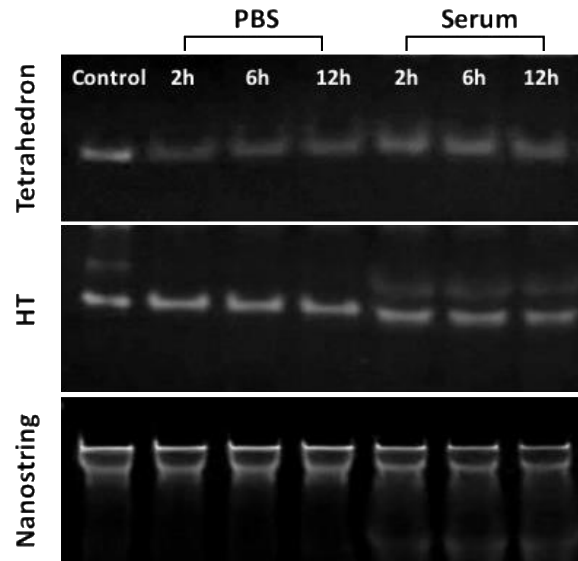


Figure S18. DNA nanostructure stability in PBS and serum. 10% Native PAGE gels show DNA nanostructures remain stable in different media over 12 hours of incubation.

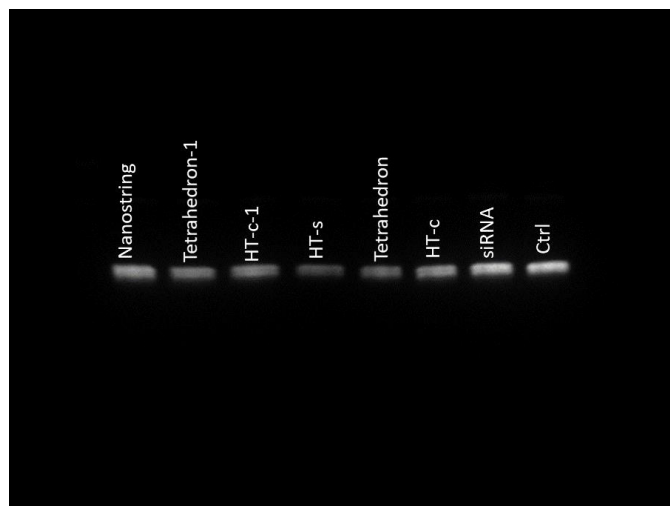


Figure S19. Representative western blot gel of GFP extracted from nanostructure-treated leaves 2-days post-infiltration.

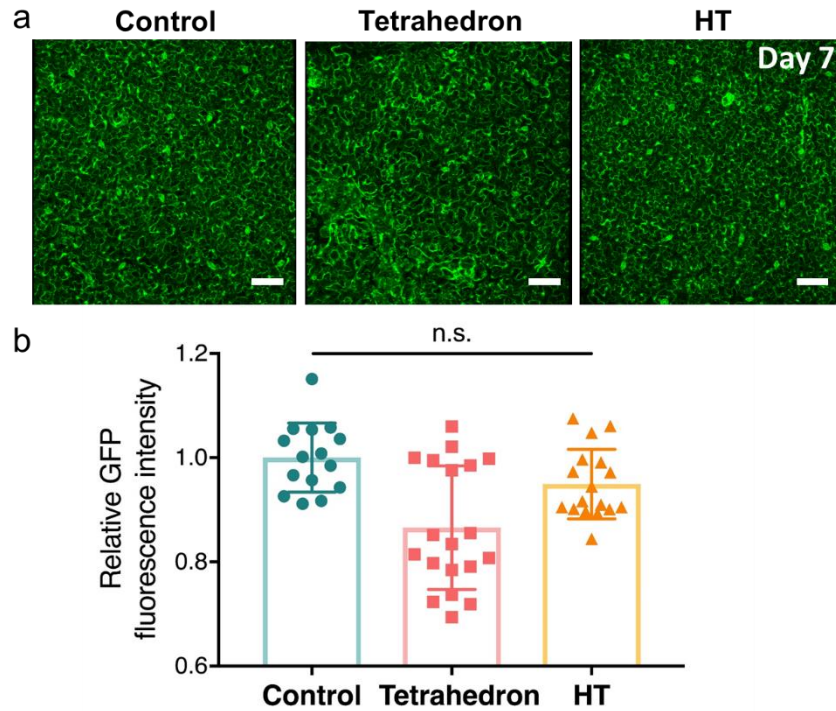


Figure S20. DNA nanostructure induced GFP silencing is transient. a) Representative confocal images of mGFP5 *Nb* leaves 7-days post-infiltration with PBS, siRNA-tetrahedron nanostructures, or siRNA-HT momomer nanostructures, showing GFP fluorescence recovery. Scale bars, 100 μ m. b) Quantitative fluorescence intensity analysis of confocal images. n.s.=non-significant (s.d. n = 15).

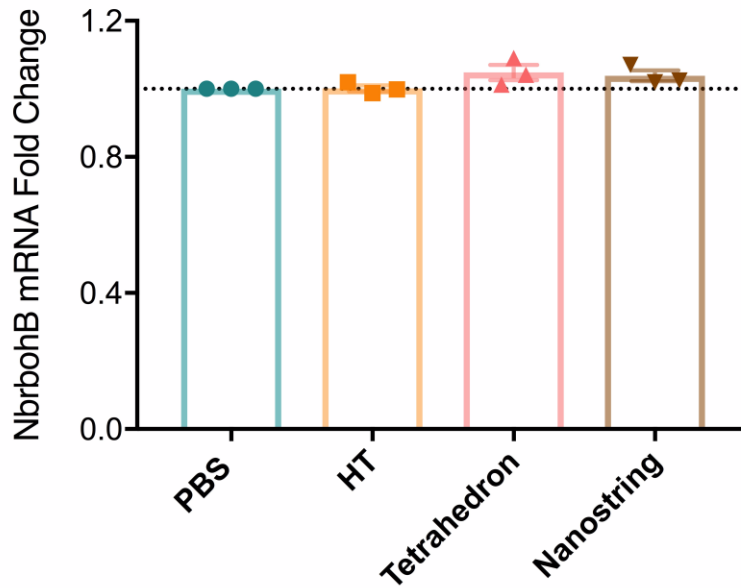


Figure S21. Plant stress gene *NbrbohB* is not upregulated by DNA nanostructures. qPCR of *NbrbohB*, a known stress gene, shows nanostructures used to deliver siRNA do not induce a stress response when infiltrated into *Nb* leaves. Error bars indicate s.e.m. (n = 3).

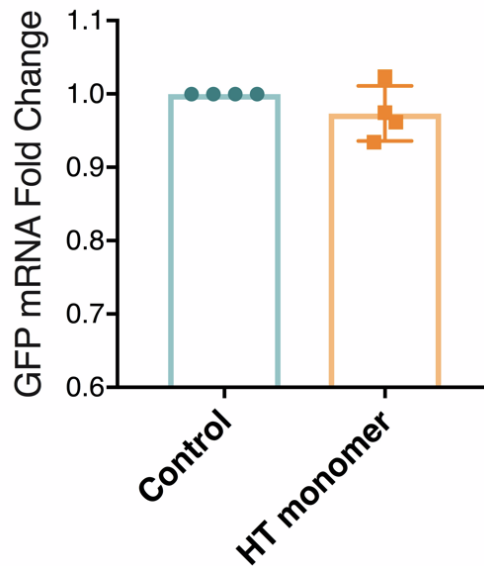


Figure S22. DNA nanostructure-induced silencing requires siRNA loading. qPCR of leaves infiltrated with HT monomer alone (no siRNA loading) 2-days post-infiltration shows no mRNA change, as expected. Error bars indicate s.e.m. (n = 4).

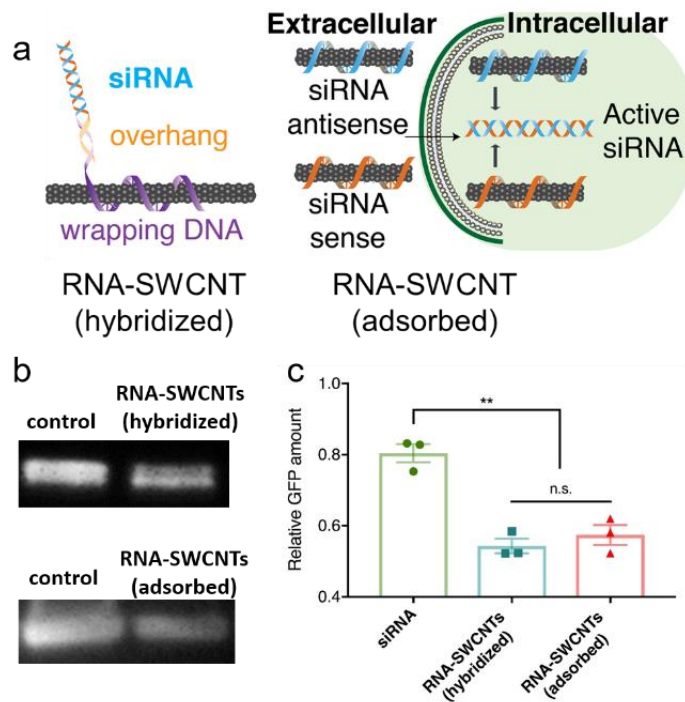


Figure S23. siRNA attachment configurations to SWCNT do not affect GFP protein silencing levels. a) Schematic of hybridization or adsorption modes for siRNA loading on SWCNTs. b) Representative western blot gel and analysis showing GFP extracted from mGFP5 *Nb* infiltrated with either free siRNA, siRNA attached SWCNTs through hybridization, or siRNA adsorbed to SWCNT 2-days post-infiltration. c) Statistical analysis showing GFP proteins extracted from different SWCNT-treated leaves 2-days post-infiltration. $P^{**} = 0.0041$ in one-way ANOVA. Error is s.e.m. ($n = 3$).

Supplementary Video S1. Mechanical stiffness calculations quantify the root mean square fluctuations (RMSF) of HT the monomer nanostructure simulated by CanDo (8, 9). White and red represent low and high relative flexibility, respectively.

Supplementary Video S2. Mechanical stiffness calculations quantify the root mean square fluctuations (RMSF) of HT the nanostring nanostructure simulated by CanDo (8, 9). White and red represent low and high relative flexibility, respectively.

Supplementary Materials and Methods

Chemicals and materials.

Super purified HiPCO SWCNTs (Lot # HS28-037) were purchased from NanoIntegris, and used for all SWCNT-based experiments. The following chemicals were purchased from Sigma-Aldrich: sodium chloride, potassium chloride, magnesium chloride hexahydrate, bovine serum albumin (heat shock fraction). Single stranded RNA and DNA oligonucleotides were purchased from and purified by Integrated DNA Technologies, Inc. (IDT); DNA oligonucleotides labeled with biotin or Cy3 were purified by HPLC, and dissolved in Milli-Q water before use. The concentration of each strand was estimated by measuring the UV absorbance at 260 nm using a UV-3600 Plus UV-Vis-NIR Spectrophotometer (Shimadzu Scientific Instruments, Columbia, U.S.A.). Streptavidin was purchased from Sigma-Aldrich Co. LLC. UltraPure DNase/RNase-free distilled water from Invitrogen was used for qPCR experiments, and EMD Millipore Milli-Q water was used for all other experiments.

Non-denaturing polyacrylamide gel electrophoresis (PAGE).

1 μ M, of a 5 μ L volume of each assembled sample was loaded onto a 10% PAGE (19:1 acrylamide/bisacrylamide in 1 \times TAE/Mg²⁺ buffer). Gels were run at 100 V (constant voltage) for two hours with an electrophoresis apparatus (Bio-rad, United States). Next, gels were stained with 1 \times SYBR[®] Gold nucleic acid dye (Thermo Fisher Scientific, United States) and scanned with a Typhoon FLA 9500 instrument (GE Healthcare life Sciences, United States of America).

AFM characterization.

2-3 μ L of the DNA nanostructure (Tetrahedron, HT monomer and nanostring) sample was deposited on a freshly cleaved mica surface and left to adsorb on the surface for 3 minutes. For AFM imaging, the mica surface was slowly rinsed with water three times (each time with 10 μ L water) to remove salt. Next, the mica surface was dried with a mild air stream by an ear-washing bulb and was imaged with a MultiMode 8 AFM with NanoScope V Controller (Bruker, Inc.) under tapping mode in air. All AFM images were analyzed by NanoScope Analysis v1.50.

Biotin-streptavidin binding assays.

The strand H1-biotin was purchased and synthesized by IDT with biotinylation at the 5' end. After the biotin labeled TH monomer or nanostrings were constructed as described above, a stoichiometric amount of streptavidin in 1 \times TAE/Mg²⁺ buffer was added, and the final molar ratio of streptavidin to biotin-nanofilament was 10:1. The mixture was left at room temperature for 5 min and then characterized by AFM as described above.

Self-assembly of DNA tetrahedral nanostructure.

Oligonucleotides A, B, C, D (see Table S1 for detailed sequences) were stoichiometrically mixed in 1×TM buffer (20 mM Tris, 50 mM MgCl₂, pH 8.0), then assembled through annealing with a PCR machine (Veriti™ 96-Well Thermal Cycler, Thermo Fisher, United States) at 95°C for 10 min, followed by cooling down to 4°C within 30 s. In detail, A-7, B-7, C-7 and D-7 assembled to form tetrahedron-7; A-26, B-26, C-26 and D-26 assembled to form tetrahedron-26; A-37-1, A-37-2, B-37-1, B-37-2, C-37-1, C-37-2, D-37-1 and D-37-2 assembled to form tetrahedron-37. For the tetrahedron with 15 nucleotide (nt) overhangs for siRNA conjugation, the A-15 stand (Table S1) was used instead of the A-7 strand. For the Cy-3 labeled tetrahedron, A-7-Cy3, A26-Cy3 and A-37-1-Cy3 were used during the annealing process instead.

Self-assembly of hairpin-tile (HT) monomer and 1D nanostring nanostructures.

Oligonucleotides H1, H2, H3, and H4 (see Table S1 for detailed sequences) were stoichiometrically mixed in a 1×TAE/Mg²⁺ buffer containing 40 mM Tris base, 20 mM acetic acid, 2 mM EDTA, and 12.5 mM magnesium acetate (pH 8.0). Next, the DNA strand solution was slowly cooled down from 95°C to 20°C over 24 hours in a water bath insulated in a Styrofoam box. To co-polymerize the 1D nanostrings, 1 μM of HT monomers A (H1, H2, H3, and H4) and B (H5, H6, H7, and H8) at equimolar concentrations were mixed with initiator strand I in a 1:0.1 ratio. The mixtures were further incubated at 20°C for 1 h and were then characterized by AFM. For the Cy3-labeled HT monomer and nanostring, Cy3-H1 was used instead of strand H1. For the HT monomer and nanostring with 15-nt overhangs with siRNA conjugation at the center, the H1-15-RNA stand was used instead of the H1 strand. For the HT monomer with 15-nt overhangs with siRNA conjugation at the side, H2-15-RNA stand was used instead of the H2 strand. For the nanostring with 15-nt overhangs for SWCNTs conjugation, the H5-15-CNT stand was used instead of the H5 strand.

Hybridization of DNA nanostructures with double stranded siRNA.

The duplex siRNA with a 15-nt overhang was synthesized by mixing two fully complementary oligonucleotides (sense-15 and antisense strands in Table S1) in 1×TAE/Mg²⁺ buffer with further incubation for 1 h at 20°C. Next, DNA nanostructures with overhangs were hybridized with the pre-formed siRNA duplex in PBS (137 mM NaCl, 2.7 mM KCl, 10 mM Na₂HPO₄, 2 mM KH₂PO₄, pH 7.4) at 37°C for 30 minutes with a final concentration of 100 nM, allowing conjugation of siRNA to the DNA nanostructures. AFM characterization of the nanostructure hybridization locus was performed by labeling each nanostructure locus with a biotin at the 5' end of the core strand. Following co-incubation of the biotinylated nanostructure with streptavidin, AFM imaging was performed.

Preparation of SWCNTs with 15-nt overhang wrapped with a DNA (GT)₁₅ -15 strand.

We designed and prepared the GT₁₅-15 wrapped SWCNTs where the 15-nt overhangs were complementary to the 15-nt overhangs on the locus of each nanostring monomer, such that the SWCNT and nanostring would hybridize to each other (see detailed sequences in Table S1 and detailed protocols in methods). To conjugate the SWCNT to the nanostring, the (GT)₁₅-15 strand was first dissolved at a concentration of 20 mg/mL in PBS buffer. 1 mg HiPCO SWCNTs was added to 400 μ L of this DNA solution, followed by probe-tip sonication with a 3-mm tip at 50% amplitude (\sim 7W) for 20 min in an ice bath. The resulting solution was next centrifuged at 16,100g for 1 h to remove unsuspended SWCNT. Unbound (free) DNA was removed via spin-filtering (Amicon, 100 K) at 1,000g for 6 minutes (5 times) and the concentration of (GT)₁₅-15 wrapped SWCNTs was determined with a UV-Vis-nIR spectrometer where SWCNT concentration was calculated in mg/L (absorbance at 632 nm/extinction coefficient of 0.036).

Conjugation of nanostrings with (GT)₁₅-15 SWCNTs.

Nanostrings with 15-nt hybridization overhangs fully complementary to the overhang of (GT)₁₅-15 were mixed with the filtered DNA wrapped SWCNTs in 0.5 \times TAE/Mg²⁺ buffer and incubated at 37°C for 30 minutes. The conjugate was characterized with AFM by next adding streptavidin to bind to and indicate the biotin labeling position along the nanostring. To better differentiate the nanostring from the SWCNTs, the same biotin-specific streptavidin strategy was employed for AFM characterization of the SWCNT-nanostring conjugate. As shown in AFM images in Fig S8, we observe discrete patterns of anchored streptavidin molecules on the surface of SWCNTs, which allowed direct visualization of the successful conjugation.

Quantitative GFP fluorescence intensity analysis of gene silencing.

Infiltrated plant leaves were prepared for confocal imaging 3-days or 7-days (depending on experiment) post-infiltration with corresponding nanomaterials by cutting a small leaf section of the infiltrated leaf tissue, and inserting the tissue section between a glass slide and cover slip of #1 thickness. 20 μ L of water was added between the glass slide and cover slip to keep the leaves hydrated during imaging. A Zeiss LSM 710 confocal microscope was used to image the plant tissue with 488 nm laser excitation and with a GFP filter cube. GFP fluorescence images were obtained at 10x magnification. Confocal imaging data was analyzed to quantify GFP expression across samples. For each sample, 4 biological replicates (4 infiltrations into 4 different plants) were performed, and for each biological replicate, 15 technical replicates (15 non-overlapping confocal fields of view from each leaf) were collected. Each field of view was analyzed with custom ImageJ analysis to quantify the GFP fluorescence intensity value for that field of view, and all 15 fields of view were then averaged to obtain a mean fluorescence intensity value for that sample. The same protocol was repeated for all 4 biological replicates (4 different plants) per sample, and

averaged again for a final fluorescence intensity value, which correlates with the GFP fluorescence intensity of the sample.

Quantitative PCR (qPCR) experiments and data analysis.

Two-step qPCR was performed to quantify GFP gene silencing in transgenic mGFP5 *Nb* plants with the following commercially-available kits: RNeasy plant mini kit (QIAGEN) for total RNA extraction from leaves, iScript cDNA synthesis kit (Bio-Rad) to reverse transcribe total RNA into cDNA, and PowerUp SYBR green master mix (Applied Biosystems) for qPCR. The target gene in our qPCR was mGFP5 (GFP transgene inserted into *Nb*), and EF1 (elongation factor 1) was chosen as the housekeeping (reference) gene. Primers (see detailed sequences in Table S1) for these genes (fGFP, rGFP, fEF1 and rEF1) were ordered from IDT and used without further purification. An annealing temperature of 60°C was used for qPCR, which was run for 40 cycles. qPCR data was analyzed by the ddCt method to obtain the normalized GFP gene expression-fold change with respect to the EF1 housekeeping gene and control sample. For each sample, qPCR was performed as 3 technical replicates (3 reactions from the same isolated RNA batch), and the entire experiment consisting of independent infiltrations and RNA extractions from different plants was repeated 4 times (4 biological replicates).

Quantitative Western Blot experiments and data analysis.

Plant leaves were harvested 72 h post-infiltration and ground in liquid nitrogen to get dry frozen powders. The frozen powders were then transferred to a tube with pre-prepared lysis buffer containing 10 mM Tris/HCl (pH 7.5), 150 mM NaCl, 1 mM EDTA, 0.1% NP-40, 5% glycerol, and 1% cocktail. After lysing at 4°C overnight, the tube was centrifuged at 10,000 rpm for 20 minutes and the supernatant containing whole proteins was collected in a new tube. After quantification of the total extracted proteins by a Pierce 660 nm Protein Assay (ThermoFisher, Prod# 22660), 0.5 µg of normalized total proteins from each sample were analyzed by 12% SDS-PAGE and blotted to a PVDF membrane. The membrane was then blocked for 1 hour using 7.5% BSA in PBST (PBS containing 0.1% Tween20) buffer and rinsed 3 times in PBST buffer, followed by overnight incubation at 4°C with the primary GFP antibody as required (1:2000 dilution, Abcam, ab290). After extensive washing, the corresponding protein bands were probed with a goat anti-rabbit horseradish peroxidase-conjugated antibody (1:5000 dilution, Abcam, ab205718) for 30 min. After 3 washes, the membrane was then developed by incubation with chemiluminescence (Amersham ECL prime kit) and imaged by a ChemiDoc™ XRS+ System (BIORAD). The intensity of GFP bands were quantified with ImageJ software. To correct for variability in protein expression across different plants and leaves, the GFP extracted from each leaf sample was normalized by the total protein recovered from that leaf tissue.

Quantitative co-localization analysis of Cy3 labeled nanomaterials with GFP

Transgenic mGFP5 *Nb* plant leaves were infiltrated with 50 μ L Cy3-labeled nanostructures to a final nanostructure concentration of 200 nM, and prepared for confocal imaging (12h for DNA materials, and 6h for carbon nanotube related materials) following infiltration. Specifically, one of the single stranded DNA overhangs on the corresponding DNA nanostructure was labeled by Cy3: the H1 strand in HT monomer and nanostring, and one of the four or eight vertices of the tetrahedron (Table S1). SWCNTs were wrapped with Cy3 labeled GT₁₅ ssDNA, and the SWCNT-nanostring hybrid was prepared via Cy3 labeling of the nanostring at the nanostring center, which was subsequently conjugated with SWCNT. All three Cy3-labeled structures were infiltrated into mGFP5 *Nb* leaves. A small leaf section of the infiltrated leaf tissue was cut, and inserted between a glass slide and cover slip of #1 thickness. 20 μ L of water was added between the glass slide and cover slip to keep the leaf sections hydrated during imaging. A Zeiss LSM 710 confocal microscope was used to image the plant tissue with two channels: 488 nm laser excitation with a GFP filter cube and 514 nm laser excitation with a Cy3 filter cube. The images were obtained with air-immersion of the objective at 20x magnification. Confocal imaging data were then analyzed to quantify the colocalization fraction between the GFP channel and the Cy3 channel across all samples (image J). For each sample, 4 biological replicates (4 infiltrations into 4 different plants) were performed, and for each biological replicate, 15 technical replicates (15 non-overlapping confocal fields of view from each leaf) were collected. Each field of view was analyzed with custom ImageJ analysis software to quantify the colocalization percentage value for that field of view, and all 15 fields of view were then averaged to obtain a mean colocalization value for that sample. The same protocol was repeated for all 4 biological replicates per sample, and averaged again for a final colocalization value, which correlates with the percent colocalization between the Cy3 and GFP channels for each sample.

Protoplast isolation from *Nb* leaves.

Protoplasts were isolated from *Nb* leaves as described by Yoo et al.(10) with some modifications. Briefly, thinly cut *Nb* leaf strips were immersed in 20 mL of enzyme solution (consisting of cellulase and macerozyme), vacuum infiltrated for an hour in the dark using a desiccator, and further incubated at 37°C for 3 hours in the dark without stirring. Undigested leaf tissue was removed by filtration with a 75 μ m nylon mesh, and the flow-through was centrifuged at 200 g for 3 min to pellet the protoplasts in a round bottom tube. Pelleted protoplasts were resuspended in 0.4 M mannitol solution (containing 15 mM MgCl₂ and 4 mM MES) with a pH of 5.7, which has similar osmolarity and pH to the protoplasts. Isolated protoplasts can be kept viable on ice for over 24 h; however, we used only freshly isolated protoplasts for all studies.

Nanostructure internalization by protoplasts.

200 μL of the 3×10^5 cells/mL protoplast suspension was mixed with 200 nM Cy3-tagged HT monomer nanostructures. The samples were tapped lightly every 15 minutes to encourage mixing and prevent protoplasts from settling at the bottom of the tube. Samples were incubated overnight at room temperature in the dark. The supernatant containing excess free nanostructures was removed without disturbing the protoplast pellet. The protoplasts were immediately resuspended in 200 μL of MMG solution. 200 μL of the protoplast suspension was transferred to a poly-L-lysine coated microwell dish and the protoplasts were allowed to settle at room temperature for 1 hour. Immediately before imaging, protoplasts were stained with 1 $\mu\text{g}/\text{mL}$ DAPI for 5 minutes and all images were captured with a fluorescence microscope using brightfield, Cy3, and DAPI channels.

Supplementary References

1. Rothmund PW, *et al.* (2004) Design and characterization of programmable DNA nanotubes. *J Am Chem Soc* 126(50):16344-16352.
2. Wang T, Schiffels D, Martinez Cuesta S, Kuchnir Fygenon D, & Seeman NC (2012) Design and characterization of 1D nanotubes and 2D periodic arrays self-assembled from DNA multi-helix bundles. *J Am Chem Soc* 134(3):1606-1616.
3. Schuller VJ, *et al.* (2011) Cellular Immunostimulation by CpG-Sequence-Coated DNA Origami Structures. *Acs Nano* 5(12):9696-9702.
4. Li J, Fan C, Pei H, Shi J, & Huang Q (2013) Smart drug delivery nanocarriers with self-assembled DNA nanostructures. *Adv Mater* 25(32):4386-4396.
5. Yoshioka H, *et al.* (2003) Nicotiana benthamiana gp91phox homologs NbrbohA and NbrbohB participate in H₂O₂ accumulation and resistance to Phytophthora infestans. *Plant Cell* 15(3):706-718.
6. Bathe M (2008) A finite element framework for computation of protein normal modes and mechanical response. *Proteins* 70(4):1595-1609.
7. Yu MF, Files BS, Arepalli S, & Ruoff RS (2000) Tensile loading of ropes of single wall carbon nanotubes and their mechanical properties. *Phys Rev Lett* 84(24):5552-5555.
8. Castro CE, *et al.* (2011) A primer to scaffolded DNA origami. *Nat Methods* 8(3):221-229.
9. Pan KY, Bricker WP, Ratanalert S, & Bathe M (2017) Structure and conformational dynamics of scaffolded DNA origami nanoparticles. *Nucleic Acids Res* 45(11):6284-6298.
10. Yoo S-D, Cho Y-H, & Sheen J (2007) Arabidopsis mesophyll protoplasts: a versatile cell system for transient gene expression analysis. *Nature protocols* 2(7):1565.